Polymer Testing 63 (2017) 168–179

Contents lists available at ScienceDirect

Polymer Testing

journal homepage: www.elsevier.com/locate/polytest

Hot tensile fracture characteristics and constitutive modelling of polyether-ether-ketone (PEEK)

Fei Chen [a, b, *], Hengan Ou [b, **], Shakir Gatea [b], Hui Long [c]

[a] National Engineering Research Centre of Die & Mold CAD, Shanghai Jiao Tong University, 1954 Huashan Road, Shanghai, 200030, China
[b] Department of Mechanical, Materials and Manufacturing Engineering, University of Nottingham, Nottingham, NG7 2RD, UK
[c] Department of Mechanical Engineering, University of Sheffield, Sheffield, S1 3JD, UK

ARTICLE INFO

Article history:
Received 19 June 2017
Received in revised form
24 July 2017
Accepted 27 July 2017
Available online 20 August 2017

Keywords:
PEEK
Hot deformation
Fracture characteristics
Constitutive modelling

ABSTRACT

The effects of strain rate and deformation temperature on the deformation behaviors of polyether-ether-ketone (PEEK) were studied by uniaxial tensile tests with the temperature range of 23–150 °C and strain rate of 0.01–1 s^{-1}. The effects of deformation temperature and strain rate on the hot tensile deformation behavior and fracture characteristics were investigated by scanning electron microscope (SEM) and discussed in detail. SEM experimental results suggest that fracture morphology is not strain rate sensitive but temperature sensitive. Based on the tensile results, the Johnson-Cook and modified Johnson-Cook constitutive models were established for PEEK. Furthermore, a comparative study has been made on the accuracy and effectiveness of the developed models to predict the flow stress. The results show that the original Johnson-Cook model reflects the deformation behavior more accurately throughout the entire test temperature and strain rate range under uniaxial tensile conditions.

1. Introduction

As a semi-crystalline, high purity polymer comprising of repeating monomers of two ether groups and a keytone group, PEEK has excellent mechanical properties maintained to high temperatures and appropriate biocompatibility [1–3]. Up to now, PEEK and its composites such as carbon fibber reinforced (CFR) and hydroxyapatite (HA) filled and/or HA coated PEEK have attracted significant interest in biomaterials for orthopaedic, trauma, spinal and dental implants in recent years [4–7].

Compared with traditional metallic and ceramic implants, PEEK has several attractive properties. On the one hand, PEEK and its composites are transparent to X-rays, show no artifacts created in CT images. On the other hand, they have shown appropriate biocompatibility and comparable elastic modulus (3–4 GPa) to human bone structures, which is beneficial for the elimination of the extent of stress shielding that is often observed in titanium-based metallic implants. Generally speaking, the researches in this field mainly focus on the following two aspects. One is the clinical performance of PEEK as a biomaterial for orthopaedic, trauma, and spinal implants. A number of investigations have been conducted to investigate on the radiolucency, *vivo* degradation and radiation sterilization, the *in vitro* response of human osteoblasts of PEEK [8,9]. The method to enhance of biocompatibility and adhesion to bone tissue by coating with a pure titanium layer on the surface of PEEK was also reported [10]. Recently, a novel method has been developed to produce a three-dimensional porous and nanostructured network on PEEK. By using this method, bioactivity, cytocompatibility, osseointegration and bone-implant bonding strength have been greatly enhanced [11]. The other aspect is related to the mechanical behaviors of PEEK. An extensive review of mechanical properties of PEEK has been provided [12]. The tensile properties have been examined by a number of authors [13–16]. At the same time, the compressive properties over a wide range of strain rates have been also studied [17,18]. Recently, the notch sensitivity [19], notched fatigue [20], mechanical impact property [21] and the effect of microstructural inclusions on fatigue life [22] of PEEK have also been studied. As in our previous study, a constitutive model was developed to describe the flow behavior of PEEK under uniaxial compression condition [23], and the effect of stress triaxiality on the fracture behavior of PEEK was also studied [24]. These works, combined with analysis of fracture surface,

* Corresponding author. National Engineering Research Centre of Die & Mold CAD, Shanghai Jiao Tong University, 1954 Huashan Road, Shanghai, 200030, China.
** Corresponding author.
E-mail addresses: feichen@sjtu.edu.cn (F. Chen), H.Ou@nottingham.ac.uk (H. Ou).

http://dx.doi.org/10.1016/j.polymertesting.2017.07.032

provide the basis for the majority of research on fracture properties of PEEK. Meanwhile, these studies give some great insights into the mechanical properties of PEEK at room temperature. However, hot deformation behavior of PEEK need to be further studied. Furthermore, no work has been attempted to the development of validated material models for numerical simulation, such as constitutive equation under tensile loading conditions. In this study, the effects of thermo-mechanical parameters on the hot tensile deformation behaviors and fracture characteristics of PEEK were studied by uniaxial tensile tests and scanning electron microscopy (SEM). A comprehensive constitutive model to describe the relationship of stress, strain rate and deformation temperature was developed and validated by experimental results.

2. Materials and experiments

The material used in this study belongs to a class of materials known as two-phase semi-crystalline polymer, consisting of an amorphous phase and a crystalline phase. PEEK 450G extruded natural rod (Röchling Group, Germany) was adopted in testing. The chemical formula of PEEK is shown in Fig. 1(a). Mechanical and thermal properties of the material are given in Table 1. The crystallinity (fraction in mass) calculated from density is 38% [25]. In addition to high resistance to gamma radiation sterilisation, high strength, good radiolucency and biocompatibility, unfilled PEEK has been widely used in both hip-joint and lumbar spinal cages and cranial implants with considerable clinical success. According to BS ISO 20753:2008, the dimension of the plate specimen can be found in Fig. 1(b).

Tensile tests of plate specimens were carried out at room temperature, 100 °C, 140 °C and 150 °C in a universal INSTRON servo hydraulic testing machine. The tests were performed at a strain rate of 0.01 s^{-1}, 0.1 s^{-1} and 1 s^{-1}. The specimens were tested inside a temperature chamber made “in house”. In order to have axial strain measurements, the specimens were instrumented with a video gauge, as shown in Fig. 2. After the hot deformation, the fracture surfaces were examined by using the scanning electron microscope (SEM) to investigate the effects of the deformation parameters on the fracture characteristics of the studied PEEK.

3. Results and discussion

3.1. Hot tensile behaviors of the studied PEEK

The true stress-true strain curve is always used to analyse the plastic deformation behaviors of materials. Fig. 3 gives the tensile true stress-true strain curves of the studied PEEK under different deformation conditions. It is obvious that the flow behaviors are heavily dependent on the deformation temperature and strain rate. At the same time, Fig. 4 shows the effects of deformation parameters on the peak stress. Obviously, the peak stress decreases with increasing the deformation temperature or decreasing the strain rate. This is because high deformation temperature enhances the thermal activation process, and low strain rate provides longer time for energy accumulation of the polymer.

3.2. Fracture morphology analysis of the studied PEEK

The fracture morphology of PEEK associated with temperature and strain rate were further clarified by SEM investigation on the failure specimens. Fig. 5 illustrates the stress state of the tensile testing by using plate specimen.

3.2.1. Effects of strain rate on fracture morphology

Figs. 6 and 7 show the fracture morphologies under the room temperature with the strain rates of 0.1 s^{-1} and 0.01 s^{-1} respectively. In case of the strain rate of 0.1 s^{-1}, the morphology is very rough, typical of ductile tearing. As shown in Fig. 7, it gives the similar morphology with the strain rate of 0.01 s^{-1}. Maybe the reason is that PEEK has a relative low crystallinity and nucleation density at room temperature. From early studies, it is known that increasing the crystallisation temperature can alter the intrinsic crystallinity of polymer which plays a crucial role in determining the deformation mechanisms of the material [26].

Fig. 6-A shows the typical parabolic shape that is very close to the pre-crack tip. The preferential direction of the parabolic is that of the ultimate crack growth. This typical pattern has previously been observed by Chu and Schultz [27] and Rae et al. [12]. Fig. 6-A (a-e) shows the detailed features from the centre to the edge of the parabolic shape. The failures initiated at randomly distributed weaker nucleation points and coalesced (Fig. 6-A-a), followed by a region of crack growth (Fig. 6-A-b). It is worth mentioning that micro-ductile tearing edges (outlined by a red dotted line) due to plastic deformation can be easily found at this region. And then, a region of striations/river markings can be found (Fig. 6-A-c). Characteristic striations/river markings representative of plastic flow have been reported by Karger-Kocsis and Friedrich [28] and Rae et al. [12]. It means that the observations in this study broadly agree with Karger-Kocsis and Friedrich and Rae observations. Finally, there is a transition region (Fig. 6-A-d) to a fast fracture region (Fig. 6-A-e). Fig. 6-B shows the morphology of fast region. It is worth noting that the region suffered intense whitening due to plastic deformation before crack. As can be seen from Fig. 6-B-b, small cavities are nucleated at the weak points of the studied polymer such as the intercrystalline zones and the boundary between the inclusions/particles and the PEEK matrix.

As shown in Fig. 7, the fracture morphologies under the strain rate of 0.01 s^{-1} is also covered with typical parabolic shape, fast fracture zone and tearing edges. It means that fracture also takes places through the process of microvoids initiation, growth and coalescence. Fig. 7-A and B show the typical parabolic shape and the fast fracture patterns respectively. Compared to Fig. 6-A, the density and thickness of striations/river markings get more pronounced in Fig. 7-A-c and d. It suggests that the density and thickness of striations/river markings increase qualitatively with decreasing of strain rate. Fig. 7-B gives the typical pattern at fast fracture zone. As shown in the figure, the pattern is near perfect disk with uniform propagation in all directions. It is because of the

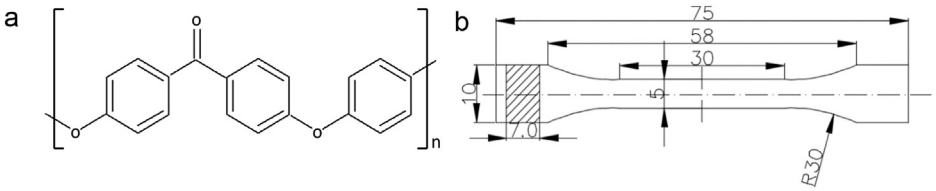

Fig. 1. (a) The chemical formula of PEEK. (b) Geometry and dimensions of the specimen (unit: mm).

Table 1
Material properties of PEEK 450G.

Mechanical properties		Thermal properties	
Elastic modulus (GPa)	3.6	Thermal conductivity (W/mK)	0.29
Poisson's ratio	0.38	Specific heat (J/kg K)	2180
Density (kg/m3) 1300	Glass transition temperature (K)	416	
Yield stress (MPa)	107	Melting temperature (K)	616

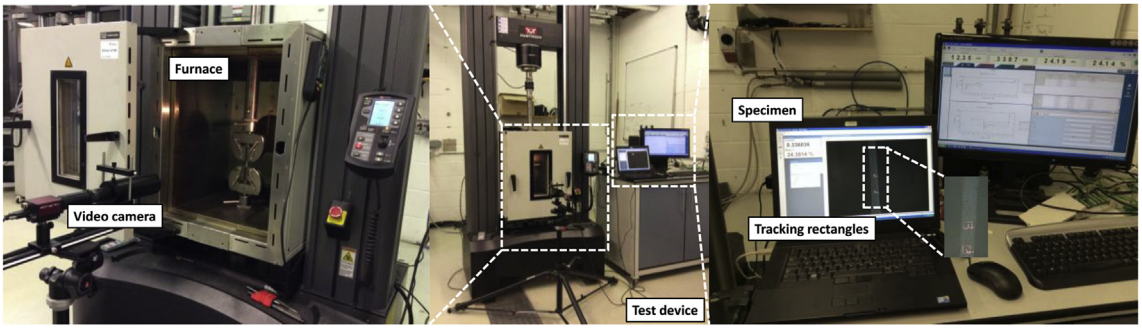

Fig. 2. Tensile device for smooth axisymmetric specimens at elevated high temperature.

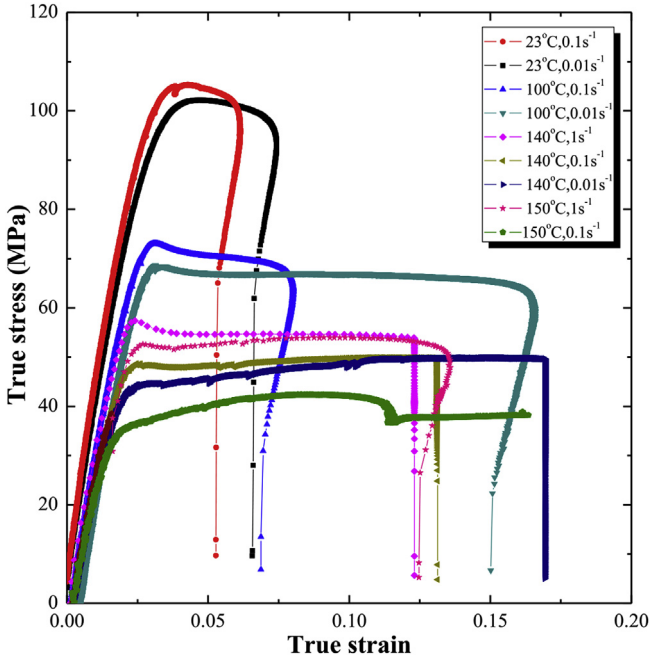

Fig. 3. The tensile true stress-true strain curves.

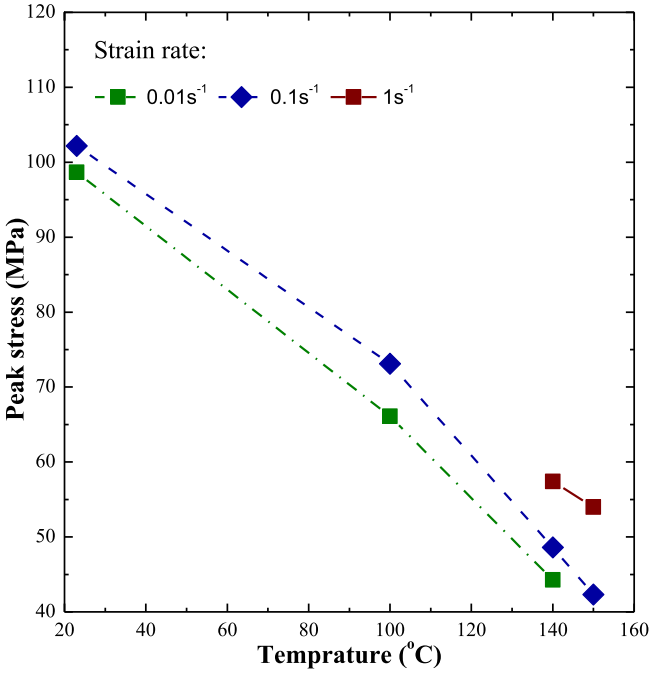

Fig. 4. Effects of deformation parameters on the peak stress.

defect-induced micro-crack in the high stress concentration region (in the centre of the specimen during deformation) due to the inclusions/particles [27].

3.2.2. *Effects of deformation temperature on fracture morphology*

Figs. 8–10 show the fracture morphologies under the deformation temperatures of 100 °C, 140 °C and 150 °C respectively. Generally, an increase in temperature results in a longer crystallisation time for spherulitic growth, which has a large impact on the hot deformation behavior of PEEK in terms of true strain-true stress curve (Fig. 3). But the temperature has limited effect on the fracture morphologies for PEEK. Going through these figures, the following interesting can be found. The striations/river markings are also very obviously. But it is not the case for the parabolic shape at the temperatures of 100 °C and 140 °C. Above the glass transition temperature (T_g), it gives a bigger parabolic feature, as shown in Fig. 10(outlined by a red dotted line). Moreover, the microscale morphology (Fig. 10-c) shows drawn mountain-like morphology at fast fracture zone. However, when the temperature is lower than T_g, this type of pattern is not obvious.

3.3. *Constitutive equation modelling*

As shown in Fig. 4, the configuration of all the tensile true stress-true strain curves is similar under all the deformation conditions [29–31]. It is concluded that the typical curve can be divided into

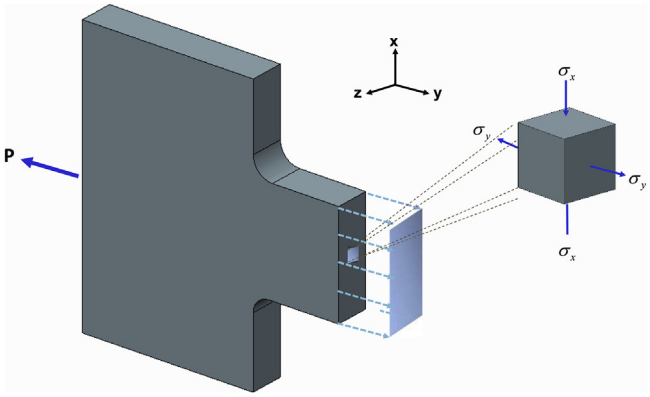

Fig. 5. State of stress in the plate tension specimen. In this case, plane stress is defined to be a state of stress in which the normal stress, σ_z, and the shear stresses, τ_{xz} and τ_{yz}, directed perpendicular to the *x*-*y* plane are assumed to be zero. It means that the loads are applied uniformly over the thickness of the plate.

four distinct stages, i.e., elastic stage (I), uniform deformation stage (II), diffusion necking stage (III) and localized necking stage (IV), as shown in Fig. 11. Firstly, the stress increases linearly with the increasing of strain in the elastic stage. Work hardening plays a dominate role in this stage. Accompanying the deformation, strain concentration/necking takes place because of the mesoscopic defects such as the initiation and growth of the microvoids and microcracks inside the material. But because of strain-rate sensitivity of the flow stress, the deformation resistance in the necking area increases and the local deformation slows down. Then the necking transfers to the sections with relatively weak deformation resistance. It results that the necking sites transfer and diffuse continuously. Moreover, it gives rise to the slow decreasing of the flow stress in the diffusion necking stage. With the further straining, the damage inside specimen becomes more and more serious, which results that the diffusion of necking cannot continue anymore. Finally, the localized necking occurs. It gives the rapid drop of the flow stress in the localized necking stage. In order to choose the appropriate forming equipment and forming parameters, such as deformation temperature and strain rate, it is desirable to predict the flow stress and further to estimate the forming behavior of the materials. Here, the aim of this section is to compare the capability of the three models to represent the flow behavior of PEEK.

3.3.1. Johnson Cook model

Among the phenomenological models, the Johnson-Cook (JC) model [32] has been successfully applied for predicting the flow stress of materials [33,34]. The JC model can be described as following:

$$\sigma = \left[A + B\left(\varepsilon_{\text{plastic}}\right)^{n}\right]\left[1 + C\ln\left(\frac{\dot{\varepsilon}}{\dot{\varepsilon}_{\text{reference}}}\right)\right] \times \left[1 - \left(\frac{T - T_{\text{reference}}}{T_{\text{melting}} - T_{\text{reference}}}\right)^{m}\right] \quad (1)$$

where σ is flow stress, A is yield stress at reference temperature and reference strain rate, B is the strain hardening coefficient, n is the strain hardening exponent, $\varepsilon_{\text{plastic}}$ is the equivalent strain, $\dot{\varepsilon}$ is strain rate and $\dot{\varepsilon}_{\text{reference}}$ is the reference strain rate, T is temperature. $T_{\text{reference}}$ is the reference temperature. T_{melting} is the melting temperature of PEEK at 616 K. In Eq. (1), C and m are coefficients of strain rate hardening and thermal softening exponent, respectively.

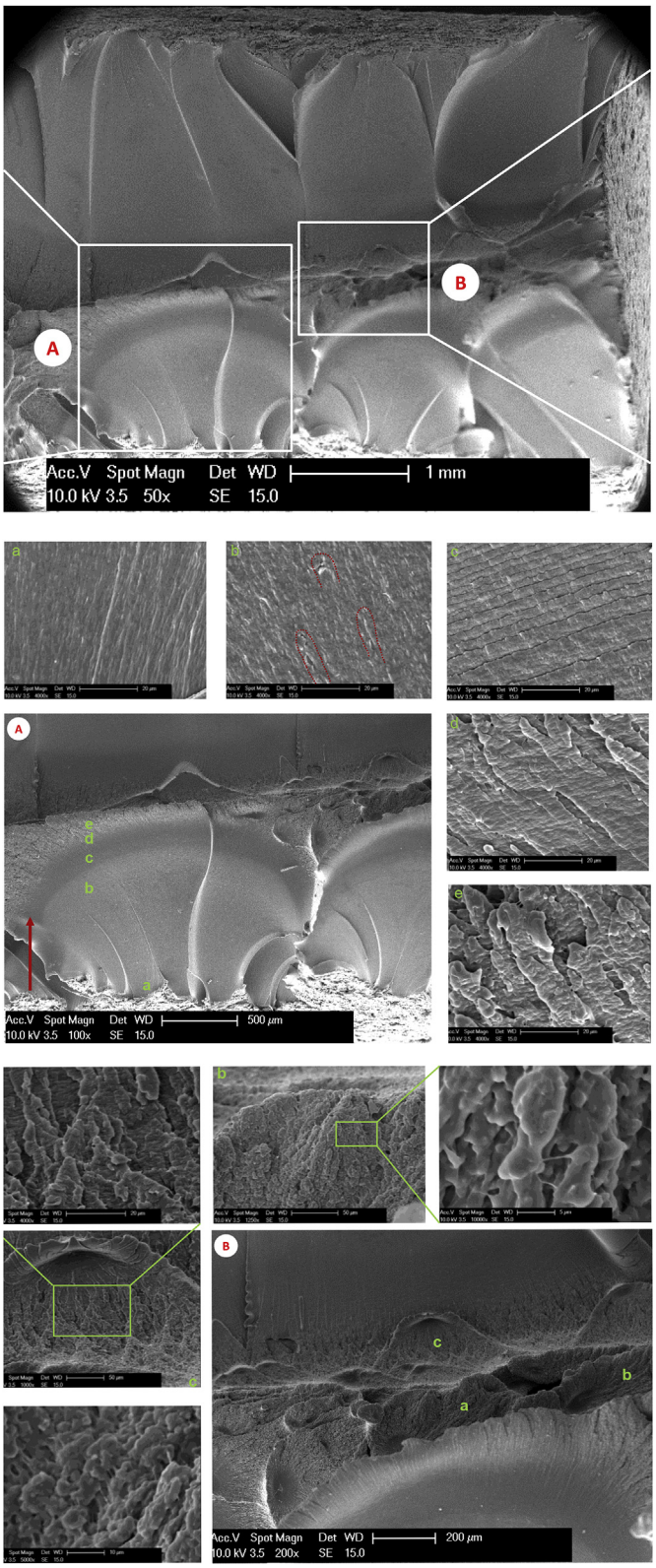

Fig. 6. SEM fractograph at room temperature with the strain rate of 0.1 s^{-1}. The arrow indicates the direction of the crack propagation.

Therefore, the total effect of strain hardening, strain rate hardening and thermal softening on flow stress can be calculated by multiplying these three terms in Eq. (1). The temperature increase

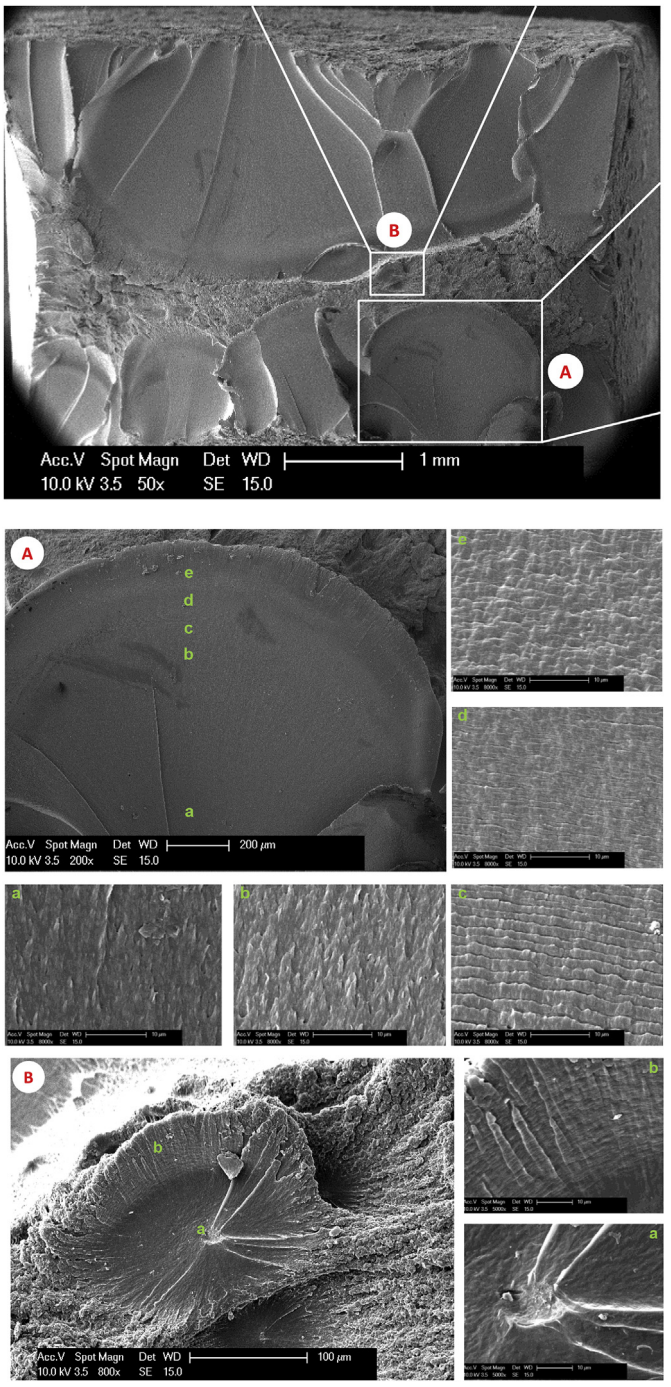

Fig. 7. SEM fractograph at room temperature with the strain rate of 0.01 s^{-1}.

caused by deformation cannot be neglected when the strain rate is relatively high. The deformation-induced temperature increase can be estimated by assuming a conversion factor of 0.9 from deformation work into heat from an initial testing temperature T_0,

$$\int_{T_0}^{T} \rho C_p dT = 0.9 \int_{0}^{\varepsilon^p} \sigma d\varepsilon \tag{2}$$

where ρ is the density, C_p is the heat capacity, and ε is the strain. Assuming ρ and C_p are constants, therefore, Eq. (2) can be rearranged to,

$$T = T_0 + \Delta T = T_0 + \int_{T_0}^{T} dT = T_0 + \frac{0.9}{\rho C_p} \int_{0}^{\varepsilon^p} \sigma d\varepsilon \tag{3}$$

In the current work, 296 K (room temperature) and 0.1s^{-1} are taken as reference temperature and reference strain rate respectively. It was found that $A = 81$ MPa. At reference temperature and strain rate, Eq. (1) can be simplified as $\sigma = A + B(\varepsilon_{plastic})^n$. Taking natural logarithm for both sides of the equation gives $\ln(\sigma - A) = \ln B + n \ln \varepsilon_{plastic}$. Therefore, the slope and intercept of the plot of $\ln(\sigma\text{-}A)$ against $\ln\varepsilon_{plastic}$ was used for obtaining the values of $n = 0.23$ and $B = 41$ MPa. At the reference temperature, Eq. (1) can also be simplified as

$$\frac{\sigma}{81 + 41\left(\varepsilon_{plastic}\right)^{0.23}} = 1 + C \ln\left(\frac{\dot{\varepsilon}}{\dot{\varepsilon}_{reference}}\right) \tag{4}$$

Therefore, the slope and the intercept of the plot of $\frac{\sigma}{81+41(\varepsilon_{plastic})^{0.23}}$ against $\ln\left(\frac{\dot{\varepsilon}}{0.1}\right)$ at constant strains and various strain rates gives the value of $C = 0.0141$. At the reference strain rate, Eq. (1) is simplified as

$$1 - \frac{\sigma}{81 + 41\left(\varepsilon_{plastic}\right)^{0.23}} = \left(\frac{T - T_{reference}}{320}\right)^{m} \tag{5}$$

Taking natural logarithm for both sides of Eq. (5) gives

$$\ln\left[1 - \frac{\sigma}{81 + 41\left(\varepsilon_{plastic}\right)^{0.23}}\right] = m \ln\left(\frac{T - T_{reference}}{320}\right) \tag{6}$$

Therefore, the slope of the plot of $\ln\left[1 - \frac{\sigma}{81+41(\varepsilon_{plastic})^{0.23}}\right]$ against $\ln\left(\frac{T-T_{reference}}{320}\right)$ at constant strains and various temperatures gives

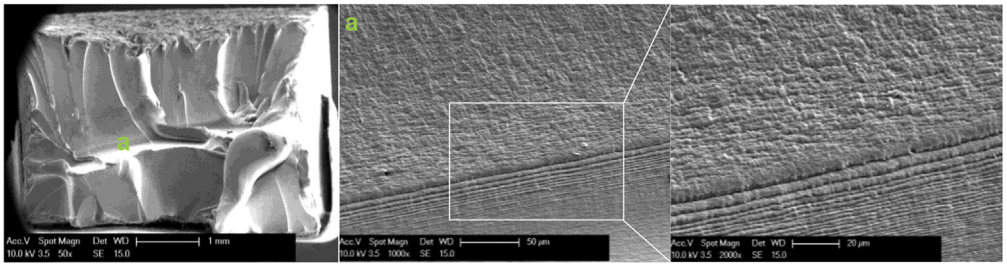

Fig. 8. SEM fractograph at the temperature of 100 °C and the strain rate of 0.01 s^{-1}.

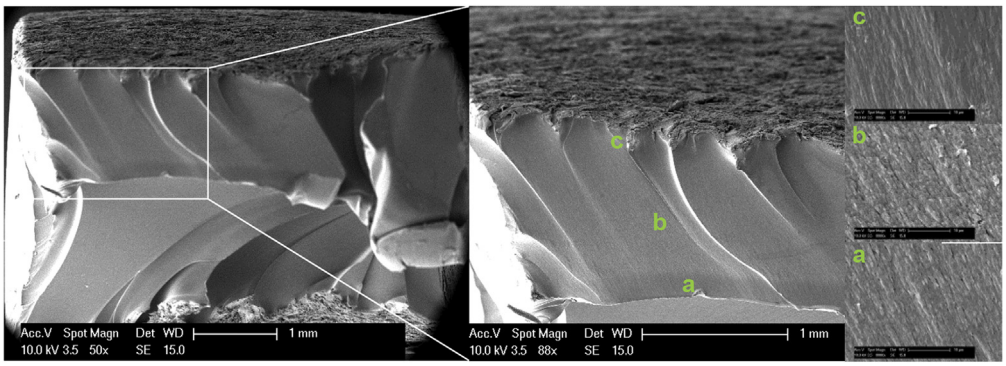

Fig. 9. SEM fractograph at the temperature of 140 °C and the strain rate of 0.01 s^{-1}.

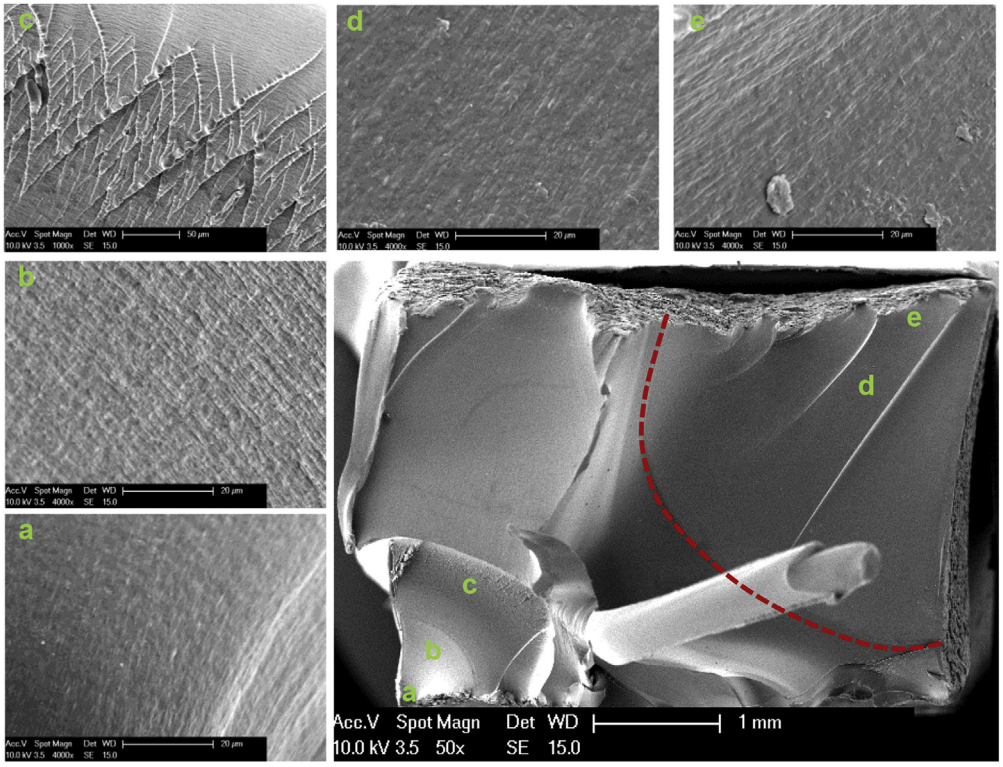

Fig. 10. SEM fractograph at the temperature of 150 °C and the strain rate of 0.1 s^{-1}.

$m = 0.76$. In the end, the JC equation can be summarized as follows;

$$\sigma = \left[81 + 41\left(\varepsilon_{\text{plastic}}\right)^{0.23}\right] \times \left(1 + 0.0141 \ln \frac{\dot{\varepsilon}}{\dot{\varepsilon}_{\text{reference}}}\right) \times \left[1 - \left(\frac{T - T_{\text{reference}}}{T_{\text{melting}} - T_{\text{reference}}}\right)^{0.76}\right] \quad (7)$$

Fig. 12 shows the comparisons between the predictions of JC model and experimental data. As can be seen from Fig. 12, in the range of temperatures from 23 °C to 150 °C, the developed JC constitutive model can give reasonable predictions of the flow stress. But it is clear that the difference becomes obvious when the temperature is higher than 140 °C with different strain rates. The bigger difference could be attributed to the change of physical properties of PEEK when the temperature is close to the glass transition temperature (T_g = 143 °C for PEEK). At this temperature range, molecular motion is sufficient to result in slow densification of amorphous phase. With the increasing of temperature, when the temperature is above T_g but below the melting temperature (T_m), chain segments in the amorphous region are sufficiently mobile to allow recrystallization, lamellar thickening and an overall increase in the perfection of the crystallites. This change in crystal characteristics can have a significant effect on the mechanical properties including flow stress.

3.3.2. *Modified JC model I*

In order to better consider the effect of temperature on the flow behavior, the modified temperature term has been developed in our previous study [23], the modified JC model is proposed as follows:

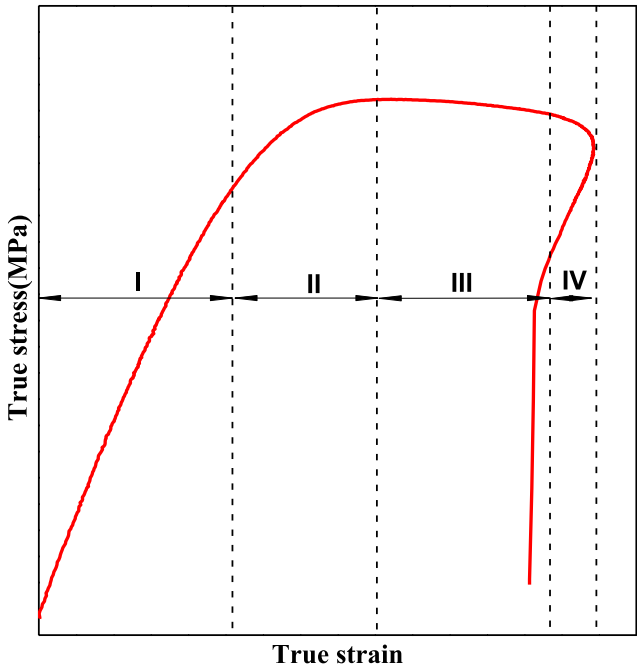

Fig. 11. Four stages of a typical true stress-true strain curve of PEEK.

$$\sigma = \left[A_2 + B_2\left(\varepsilon_{\text{plastic}}\right)^{n_2}\right]\left[1 + C_2 \ln\left(\frac{\dot{\varepsilon}}{\dot{\varepsilon}_{\text{reference}}}\right)\right] \times \left(1 - \delta_2 \frac{e^{T/T_{\text{melting}}} - e^{T_{\text{room}}/T_{\text{melting}}}}{e - e^{T_{\text{room}}/T_{\text{melting}}}}\right) \tag{8}$$

whereA_2, B_2, C_2 and δ_2 are material constants. Following above method in Section 3.3.1, A_2, B_2, n_2 and C_2 can be obtained as 81 MPa, 41 MPa, 0.23 and 0.0141 respectively. Thus, Eq. (8) gives

$$1 - \frac{\sigma}{\left[A_2 + B_2\left(\varepsilon_{\text{plastic}}\right)^{n_2}\right]\left[1 + C_2 \ln\left(\frac{\dot{\varepsilon}}{\dot{\varepsilon}_{\text{reference}}}\right)\right]} = \delta_2 \frac{e^{T/T_{\text{melting}}} - e^{T_{\text{room}}/T_{\text{melting}}}}{e - e^{T_{\text{room}}/T_{\text{melting}}}} \tag{9}$$

Therefore, the slope of the plot of $1 - \frac{\sigma}{[A_2+B_2(\varepsilon_{\text{plastic}})^{n_2}]\left[1+C_2 \ln\left(\frac{\dot{\varepsilon}}{\dot{\varepsilon}_{\text{reference}}}\right)\right]}$ against $\frac{e^{T/T_{\text{melting}}} - e^{T_{\text{room}}/T_{\text{melting}}}}{e - e^{T_{\text{room}}/T_{\text{melting}}}}$ gives $\delta_2 = 1.0565$.

The modified JC constitutive model can be summarized as follows:

$$\sigma = \left[81 + 41\left(\varepsilon_{\text{plastic}}\right)^{0.23}\right]\left[1 + 0.0141 \ln\left(\frac{\dot{\varepsilon}}{\dot{\varepsilon}_{\text{reference}}}\right)\right] \times \left(1 - 1.0565 \frac{e^{T/T_{\text{melting}}} - e^{T_{\text{room}}/T_{\text{melting}}}}{e - e^{T_{\text{room}}/T_{\text{melting}}}}\right) \tag{10}$$

Fig. 13 gives the comparisons between the predictions of the modified JC model and experimental data. However, as shown in Fig. 13, the maximum deviation is 16%. It means that the modified JC model shows poor ability to predict the flow behavior at elevated temperature under uniaxial tensile conditions.

3.3.3. Modified JC model Π

As a matter of fact, both original JC model and modified one cannot reflect the accumulation effect of strain, strain rate and temperature, but just simply the effect of the three influencing factors are mutually independent. This assumption helps to work out the necessary material constants by only a few data and thus reduce the times of experiments. In order to overcome the insufficient of the JC model, Lin et al. established an improved JC model [36]:

$$\sigma = \left[A_3 + B_3\left(\varepsilon_{\text{plastic}}\right)^{n_3}\right]\left[1 + C_3 \ln\left(\frac{\dot{\varepsilon}}{\dot{\varepsilon}_{\text{reference}}}\right)\right] \times \exp\left[\left(\lambda_1 + \lambda_2 \ln\left(\frac{\dot{\varepsilon}}{\dot{\varepsilon}_{\text{reference}}}\right)\right)\left(\frac{T - T_{\text{reference}}}{T_{\text{melting}} - T_{\text{reference}}}\right)\right] \tag{11}$$

Following above method in Section 3.3.1, A_3, B_3, n_3 and C_3 can be obtained as 81 MPa, 41 MPa, 0.23 and 0.0141 respectively. By introducing a new parameter λ, where $\lambda = \lambda_1 + \lambda_2 \ln\left(\frac{\dot{\varepsilon}}{0.1}\right)$, Eq. (11) is simplified as,

$$\frac{\sigma}{\left[81 + 41\left(\varepsilon_{\text{plastic}}\right)^{0.23}\right]\left[1 + 0.0141 \ln\left(\frac{\dot{\varepsilon}}{0.1}\right)\right]} = \exp\left[\lambda\left(\frac{T - T_{\text{reference}}}{320}\right)\right] \tag{12}$$

Taking natural logarithm for both sides of Eq. (12) gives

$$\ln\left[\frac{\sigma}{\left[81 + 41\left(\varepsilon_{\text{plastic}}\right)^{0.23}\right]\left[1 + 0.0141 \ln\left(\frac{\dot{\varepsilon}}{0.1}\right)\right]}\right] = \lambda\left(\frac{T - T_{\text{reference}}}{320}\right) \tag{13}$$

Therefore, the slope of the plot of $\ln\left[\frac{\sigma}{[81+41(\varepsilon_{\text{plastic}})^{0.23}]\left[1+0.0141 \ln\left(\frac{\dot{\varepsilon}}{0.1}\right)\right]}\right]$ against $\left(\frac{T-T_{\text{reference}}}{320}\right)$ over the entire range of deformation temperature, strain rate and strain give three values of λ. Then $\lambda_{\dot{\varepsilon}=0.01}$, $\lambda_{\dot{\varepsilon}=0.1}$ and $\lambda_{\dot{\varepsilon}=1}$ can be evaluated as −0.8905, −0.9322, and −1.8228. As λ is a function of strain rate, $\lambda_1$and λ_2 can be calculated as −1.2151 and −0.2024 from the plot λ against $\ln\left(\frac{\dot{\varepsilon}}{0.1}\right)$ as the intercept and slope respectively. The modified JC constitutive model Π can be summarized as follows:

$$\sigma = \left[81 + 41\left(\varepsilon_{\text{plastic}}\right)^{0.23}\right]\left[1 + 0.0141 \ln\left(\frac{\dot{\varepsilon}}{\dot{\varepsilon}_{\text{reference}}}\right)\right] \times \exp\left[\left(-1.2151 - 0.2024 \ln\left(\frac{\dot{\varepsilon}}{\dot{\varepsilon}_{\text{reference}}}\right)\right) \times \left(\frac{T - T_{\text{reference}}}{T_{\text{melting}} - T_{\text{reference}}}\right)\right] \tag{14}$$

Fig. 14 shows the comparisons between the predictions of modified JC model and experimental data. As can be seen from the figure, the maximum deviation is 21%. Compared with these two models, the modified JC model Π shows poorer ability to predict the flow behavior at elevated high temperature. The reason is not quite

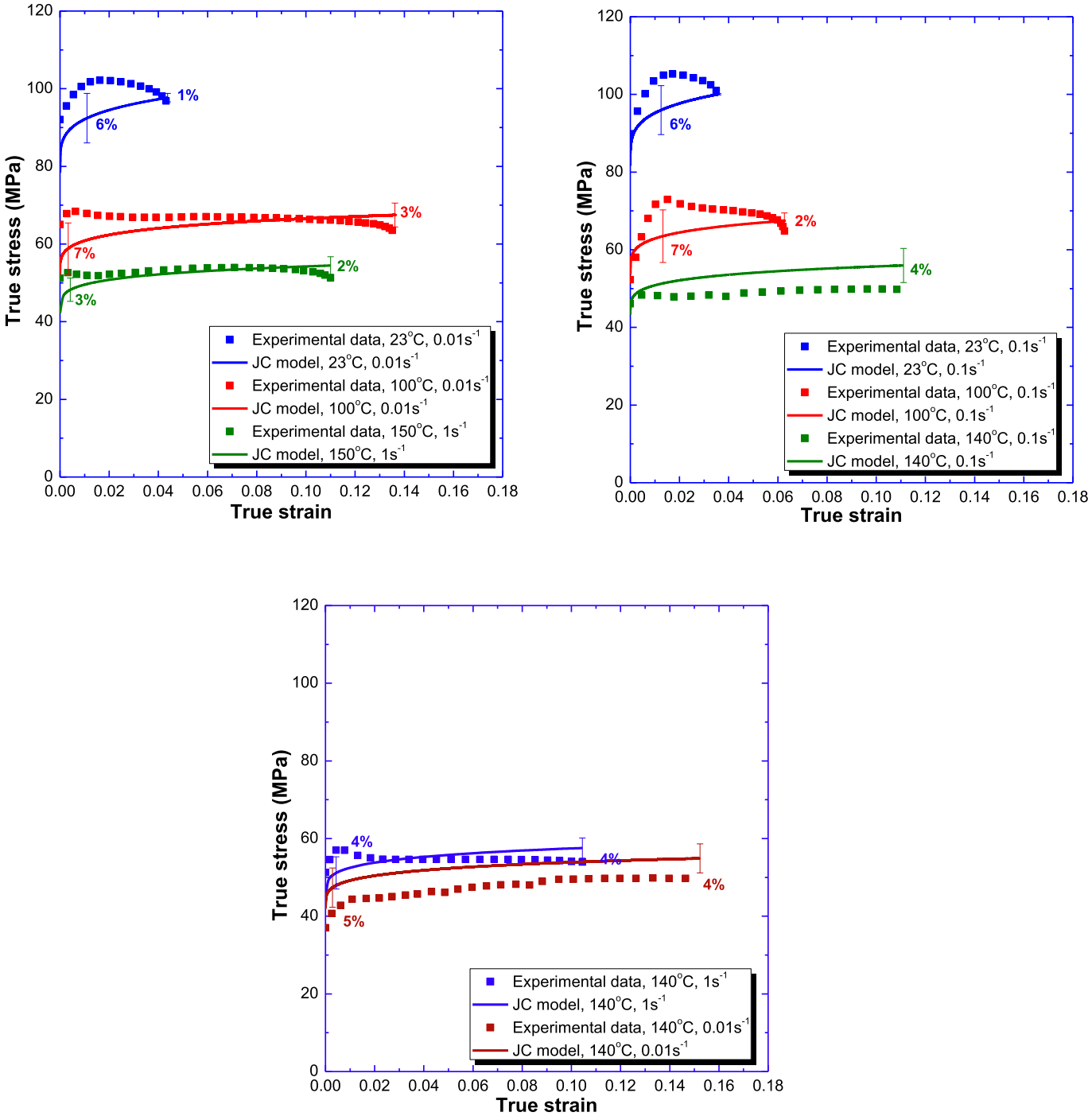

Fig. 12. Comparisons between the experimental and the calculated flow curves by the original JC model.

clear to us. Possibly, as mentioned above (in Section 3.3.1), further research needs to be done to develop an internal variable based flow stress model.

3.3.4. Analysis of the prediction accuracy

In order to further evaluate the prediction accuracy of the developed constitutive models, the predictability of the equations are quantified in terms of standard statistical parameters such as the average absolute relative error (AARE) and correlation coefficient (R) [35]. They are expressed as:

$$\mathrm{AARE}(\%) = \frac{1}{N}\sum_{i=1}^{N}\left|\frac{\sigma_{expr}^{i} - \sigma_{pred}^{i}}{\sigma_{expr}^{i}}\right| \times 100 \tag{15}$$

$$R = \frac{\sum_{i=1}^{N}\left(\sigma_{expr}^{i} - \overline{\sigma}_{expr}\right)\left(\sigma_{pred}^{i} - \overline{\sigma}_{pred}\right)}{\sqrt{\sum_{i=1}^{N}\left(\sigma_{expr}^{i} - \overline{\sigma}_{expr}\right)^{2}}\sqrt{\sum_{i=1}^{N}\left(\sigma_{pred}^{i} - \overline{\sigma}_{pred}\right)^{2}}} \tag{16}$$

where σ_{expr}^{i} is the measured data, σ_{pred}^{i} is the predicted value. $\overline{\sigma}_{expr}$

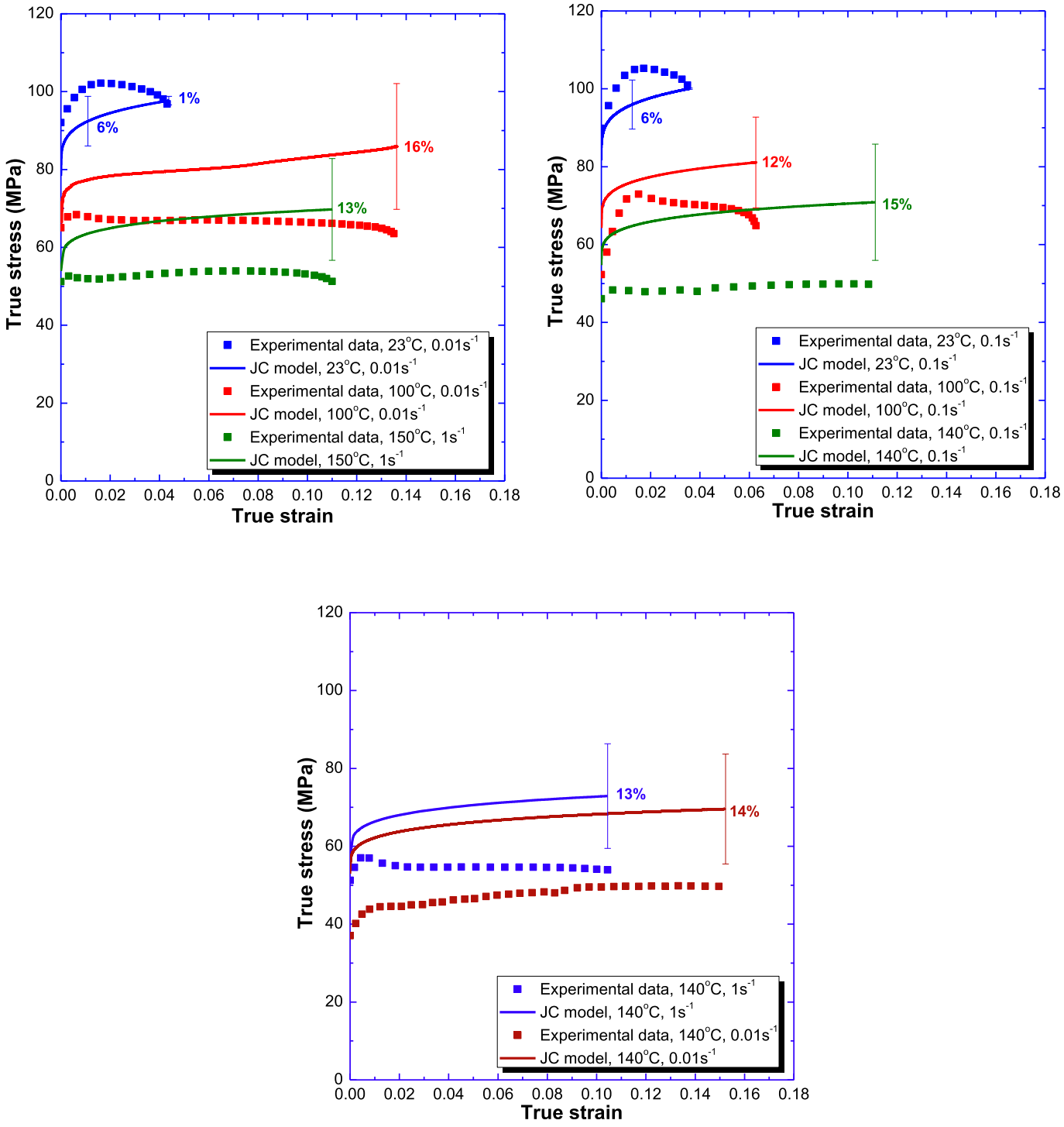

Fig. 13. Comparison between the experimental and the calculated flow curves by the modified JC model I.

and $\overline{\sigma}_{pred}$ are the mean values of σ^i_{expr} and σ^i_{pred}, respectively. N is the total number of data used in the investigation. Fig. 15 shows the comparisons between the experimental data and predicted values calculated by the three developed models. As can be seen from the figure, it is clearly that most of the data points lie very close to the line. The correlation coefficients for the original JC model, modified JC model I and modified JC model Π are 0.98, 0.95 and 0.88, respectively. The results shows that the original JC model has better correlation between the predicted results and experimental data compared with the modified ones.

In this study, it is worth noting that the developed phenomenological constitutive models predict the flow stress by using mathematical functions. The notable feature of phenomenological constitutive model is that they employ a limited number of material constants which can be easily calibrated. However, this modelling method is lack of physical background and just fits experimental observations. But usually the microstructures of PEEK consists of amorphous phase and crystalline phase change greatly depending

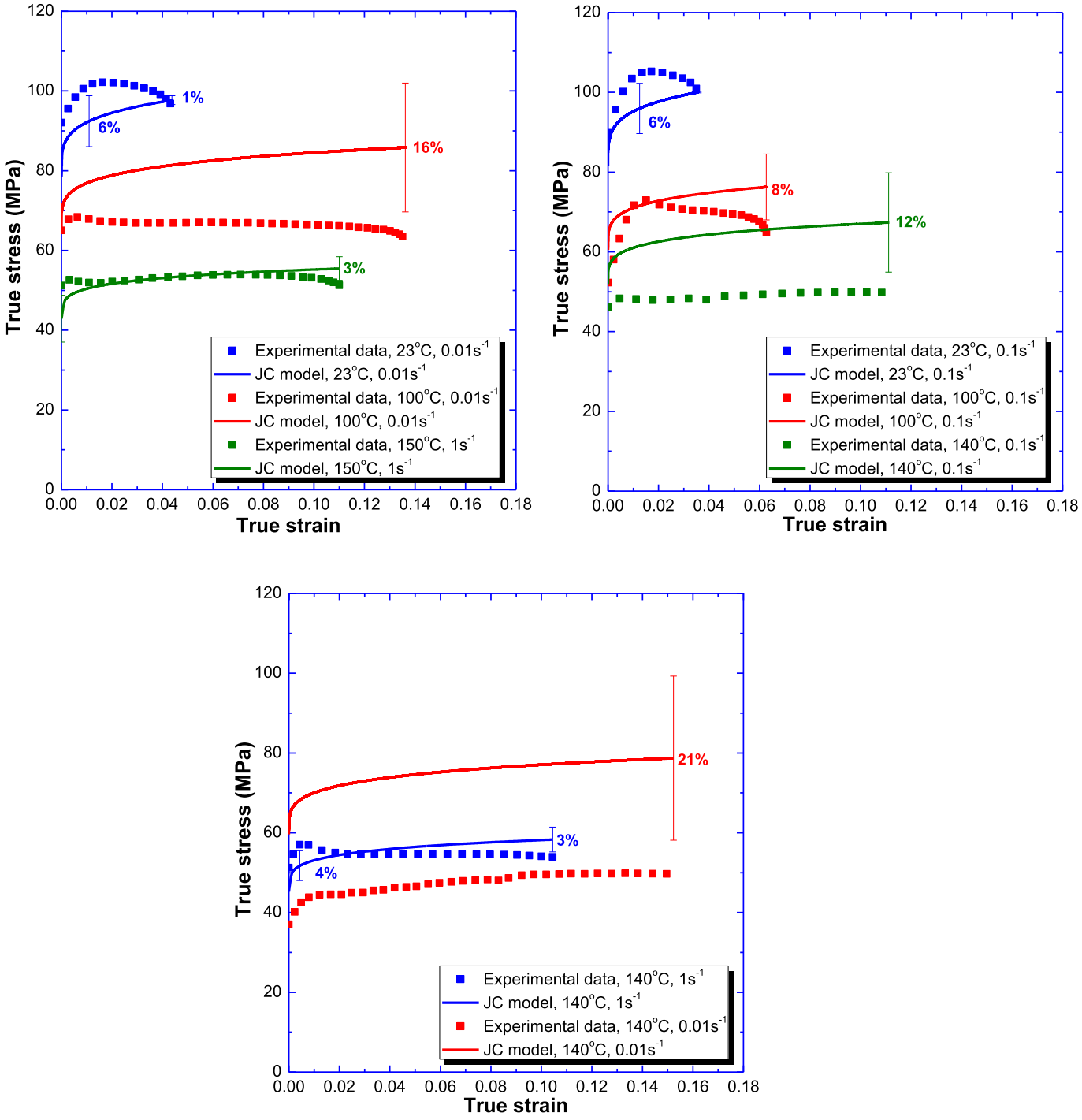

Fig. 14. Comparison between the experimental and the calculated flow curves by the modified JC model II.

on the temperature and strain rate. The change in microstructure has an essential role in flow behavior of PEEK. Therefore, it is desirable to develop physical-based constitutive models that can account for physical aspects of the material behaviors [37]. Most of them are involved in the theory of thermodynamics, crystallization of polymer and phase separation in polymer. Compared to the traditional phenomenological models, they always give an accurate definition of material behavior under wide ranges of loading conditions in terms of some physical assumptions and a larger number of material constants.

4. Conclusion

In the present work, the hot tensile deformation behaviors of PEEK are studied by uniaxial tensile tests. The effects of deformation temperature and strain rate on the fracture characteristics are discussed. Based on the experimental data, constitutive models are proposed to describe the flow behavior of PEEK. Some conclusions can be made as follows.

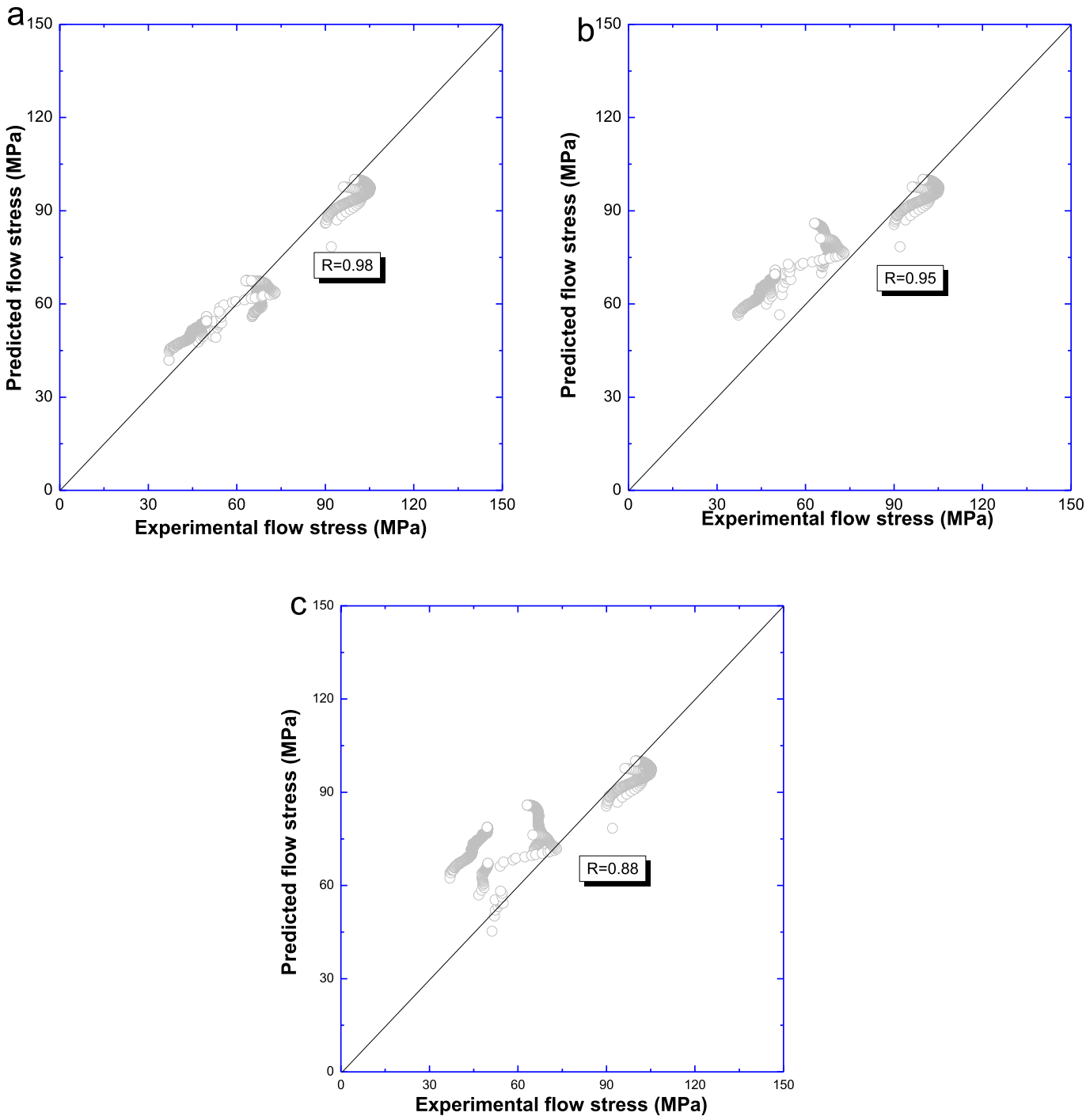

Fig. 15. Correlation between the experimental data and the predicted flow stress calculated by (a) the original Johnson-Cook model; (b) the modified Johnson-Cook model I and (c) the modified Johnson-Cook model II.

(1) Due to competitive processes of work hardening, dynamic softening and the development of voids/cracks inside the material, the tensile true stress-true strain curves of the studied PEEK can be divided into four distinct stages. Meanwhile, the flow stress decreases with the increase of deformation temperature or the decrease of strain rate.
(2) SEM experimental results suggest that fracture morphology is not strain rate sensitive but temperature sensitive. At the length scale of the crystalline spherulite, the striations/river marking is a common fracture model independent of temperature and strain rate.
(3) The established original JC constitutive model has better prediction accuracy and can provide theoretical basis for optimizing hot forming processing of the studied polymer. It correlates well with the experimental data in the entire range of temperatures and strain rates. But it is hard to consider the change of microstructure by using the developed phenomenological model. Therefore, it is deserved to

establish the physical-based constitutive model to describe the flow behavior of PEEK over the whole temperature range.

Acknowledgement

This work was supported by the Engineering and Physical Science Research Council [EP/K029592/1, EP/L02084X/1]; and the International Research Staff Exchange Scheme [IRSES, MatProFuture project, 318,968] within the 7th European Community Framework Programme (FP7).

References

[1] D.J. Blundell, B.N. Osborn, The morphology of poly (aryl-ether ether-ketone), Polymer 25 (1983) 953–958.
[2] X. Tardif, B. Pignon, N. Boyard, J.W.P. Schmelzer, V. Sobotka, D. Delaunay, C. Schick, Experimental study of crystallization of PolyEtherEtherKetone (PEEK) over a large temperature range using a nano-calorimeter, Polym. Test. 36 (2014) 10–19.
[3] M.K. Steven, PEEK Biomaterials Handbook, William Andrew, 2012.
[4] B.J. Meenan, C. McClorey, M. Akay, Thermal analysis studies of poly (ether-etherketone)/hydroxyapatite biocomposite mixtures, J. Mater. Sci. Mater. Med. 11 (2000) 481–489.
[5] N.T. Evans, F.B. Torstrick, C.S.D. Lee, K.M. Dupont, D.L. Safranski, W.A. Chang, A.E. Macedo, A.S.P. Lin, J.M. Boothby, D.C. Whittingslow, R.A. Carson, R.E. Guldberg, K. Gall, High-strength, surface-porous polyether-ether-ketone for load-bearing orthopedic implants, Acta Biomater. 13 (2015) 159–167.
[6] A.G. Kulkarni, H.T. Hee, H.K. Wong, Soliscage (PEEK) for anterior cervical fusion: preliminary radiological results with emphasis on fusion and subsidence, Spine J. 7 (2007) 205–209.
[7] J.M. Toth, M. Wang, B.T. Estes, J.L. Scifert, H.B. Seim III, A.S. Turner, Polyetheretherketone as a biomaterial for spinal applications, Biomaterials 27 (2006) 324–334.
[8] K.P. Baidya, S. Ramakrishna, M. Rahman, Quantitative radiographic analysis of fiber reinforced polymer composites, J. Biomater. Appl. 15 (2001) 279–289.
[9] K.B. Sagomonyants, M.L. Jarman-Smith, J.N. Devine, M.S. Aronow, G.A. Gronowicz, The in vitro response of human osteoblasts to polyetheretherketone (PEEK) substrates compared to commercially pure titanium, Biomaterials 29 (2008) 1563–1572.
[10] C.-M. Han, E.-J. Lee, H.-E. Kim, Y.-H. Koh, K.N. Kim, Y. Ha, S.-U. Kuh, The electron beam deposition of titanium on polyetheretherketone (PEEK) and the resulting enhanced biological properties, Biomaterials 31 (2010) 3465–3470.
[11] Y. Zhao, H.M. Wong, W.H. Wang, P.H. Li, Z.S. Xu, E.Y.W. Chong, C.H. Yan, K.W.K. Yeung, P.K. Chu, Cytocompatibility, osseointegration, and bioactivity of three-dimensional porous and nanostructured network on polyetheretherketone, Biomaterials 34 (2013) 9264–9277.
[12] P.J. Rae, E.N. Brown, E.B. Orler, The mechanical properties of poly (ether-ether-ketone) (PEEK) with emphasis on the large compressive strain response, Polymer 48 (2007) 598–615.
[13] A. Dahoun, M. Aboulfaraj, C. G'Sell, A. Molinari, G.R. Canova, Plastic behavior and deformation textures of poly (etherether ketone) under uniaxial tension and simple shear, Polym. Eng. Sci. 35 (1995) 317–330.
[14] N.D. Alberola, P. Mele, C. Bas, Tensile mechanical properties of PEEK films over a wide range of strain rates II, J. Appl. Polym. Sci. 64 (1997) 1053–1059.
[15] F. El Halabia, J.F. Rodriguez, L. Rebolledo, E. Hurtósb, M. Doblaré, Mechanical characterization and numerical simulation of polyether-ether-ketone (PEEK) cranial implants, J. Mech. Behav. Biomed. Mater 4 (2011) 1819–1832.
[16] M. Berer, Z. Major, G. Pinter, D.M. Constantinescu, L. Marsavina, Investigation of the dynamic mechanical behavior of polyetheretherketone (PEEK) in the high stress tensile regime, Mech. Time-Depend. Mater 18 (2014) 663–684.
[17] S.M. Walley, J.E. Field, P.H. Pope, N.A. Safford, The rapid deformation behaviour of various polymers, J. Phys. III 1 (1991) 1889–1925.
[18] S. Hamdan, G.M. Swallowe, The strain-rate and temperature dependence of the mechanical properties of polyetherketone and polyetheretherketone, J. Mater. Sci. 31 (1996) 1415–1423.
[19] M.C. Sobieraj, S.M. Kurtz, C.M. Rimnac, Notch sensitivity of PEEK in monotonic tension, Biomaterials 30 (2009) 6485–6494.
[20] M.C. Sobieraj, J.E. Murphy, J.G. Brinkman, S.M. Kurtz, Notched fatigue behavior of PEEK, Biomaterials 31 (2010) 9156–9162.
[21] D. Garcia-Gonzalez, A. Rusinek, T. Jankowiak, A. Arias, Mechanical impact behavior of polyether-ether-ketone (PEEK), Compos. Struct. 124 (2015) 88–89.
[22] J. Simsiriwong, R. Shrestha, N. Shamsaei, M. Lugo, R.D. Moser, Effects of microstructural inclusions on fatigue life of polyether ether ketone (PEEK), J. Mech. Behav. Biomed. Mater 51 (2015) 388–397.
[23] F. Chen, H. Ou, B. Lu, H. Long, A constitutive model of polyether-ether-ketone (PEEK), J. Mech. Behav. Biomed. Mater 53 (2016) 427–433.
[24] F. Chen, S. Gatea, H. Ou, B. Lu, H. Long, Fracture characteristics of PEEK at various stress triaxialities, J. Mech. Behav. Biomed. Mater 64 (2016) 173–186.
[25] C. Bas, A.C. Grillet, F. Thimon, N.D. Albérola, Crystallization kinetics of poly (Aryl ether ether ketone):time-temperature-transformation and continuous-cooling -transformation diagrams, Eur. Polym. J. 31 (1995) 911–921.
[26] A.A. Mehmet-Alkan, J.N. Hay, The crystallinity of poly (ether ether ketone), Polymer 33 (1992) 3527–3530.
[27] J.N. Chu, J.M. Schultz, The influence of microstructure on the failure behaviour of PEEK, J. Mater. Sci. 25 (1990) 3746–3752.
[28] J. Karger-Kocsis, K. Friedrich, Temperature and strain-rate effects on the fracture toughness of poly (ether ether ketone) and its short glass-fibre reinforced composite, Polymer 27 (1986) 1753–1760.
[29] D.D. Chen, Y.C. Lin, Y. Zhou, M.S. Chen, D.X. Wen, Dislocation substructures evolution and an adaptive-network-based fuzzy inference system model for constitutive behavior of a Ni-based superalloy during hot deformation, J. Alloys Compd. 708 (2017) 938–946.
[30] Y.C. Lin, F.Q. Nong, X.M. Chen, D.D. Chen, M.S. Chen, Microstructural evolution and constitutive models to predict hot deformation behaviors of a nickel-based superalloy, Vaccum 137 (2017) 104–114.
[31] Y.C. Lin, D.X. Wen, M.S. Chen, Y.X. Liu, X.M. Chen, X. Ma, Improved dislocation density based models for describing hot deformation behaviors of a Ni-based superalloy, J. Mater. Res. 31 (2016) 2415–2429.
[32] G.R. Johnson, W.H. Cook, Fracture characteristics of three metals subjected to various strains, strain rates, temperatures and pressures, Eng. Fract. Mech. 21 (1985) 31–48.
[33] Y.C. Lin, X.M. Chen, G. Liu, A modified Johnson-Cook model for tensile behaviors of typical high-strength alloy steel, Mater. Sci. Eng. A 527 (2010) 6980–6986.
[34] Y.C. Lin, X.M. Chen, A critical review of experimental results and constitutive descriptions for metal and alloy in hot working, Mater. Des. 32 (2011) 1733–1759.
[35] M.R. Rokni, A. Zarei-Hanzaki, A.A. Roostaei, Constitutive base analysis of a 7075 aluminium alloy during hot compression testing, Mater. Des. 32 (2011) 4955–4960.
[36] Y.C. Lin, X.M. Chen, A combined Johnson-Cook and Zerili-Armstrong model for hot compressed typical high-strength alloy steel, Comput. Mater. Sci. 49 (2010) 628–633.
[37] D. Garcia-Gonzalez, R. Zaera, A. Arias, A hyperelastic-thermoviscoplastic constitutive model for semi-crystalline polymers: application to PEEK under dynamic loading conditions, Int. J. Plast. 88 (2017) 27–52.